Showcasing research from Prof. Yuichi Negishi's laboratory, Tohoku University, Japan.

Designed construction of two new atom-precise three-dimensional and two-dimensional Ag_{12} cluster-assembled materials

This study elucidates how the binding with the organic linkers alters the symmetry of the silver nanoclusters (NCs). Changes in the symmetry of discrete NCs to assembled structures have not been reported yet. This study provides an atomic-level explanation of the transformation of symmetry from NCs to extended structures.

As featured in:

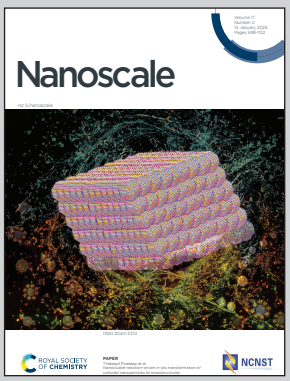

See Saikat Das, Yuichi Negishi *et al.*, *Nanoscale*, 2025, **17**, 813.

ROYAL SOCIETY OF CHEMISTRY

rsc.li/nanoscale

Registered charity number: 207890

Nanoscale

PAPER

View Article Online
View Journal | View Issue

Cite this: *Nanoscale*, 2025, **17**, 813

Designed construction of two new atom-precise three-dimensional and two-dimensional Ag_{12} cluster-assembled materials†

Riki Nakatani, [a] Jin Sakai,[a] Aishik Saha,[b] Ayumu Kondo,[a] Rina Tomioka,[a] Tokuhisa Kawawaki, [a] Saikat Das *[a] and Yuichi Negishi *[a,c]

Received 30th September 2024,
Accepted 18th November 2024

DOI: 10.1039/d4nr03992k

rsc.li/nanoscale

Silver cluster-assembled materials (SCAMs) are well-defined crystalline extended materials hallmarked by their unique geometric structures, atomically precise designability and functional modularity. In this study, we report for the first time the synthesis of a (3,6)-connected three-dimensional (3D) SCAM, $[Ag_{12}(S^tBu)_6(CF_3COO)_6(TPMA)_6]_n$ (designated as **TUS 6**), TPMA = tris(pyridine-4-ylmethyl)amine, by assembling Ag_{12} cluster nodes with the help of a tritopic linker TPMA. Besides, we also prepared a two-dimensional (2D) SCAM, $[Ag_{12}(S^tBu)_6(CF_3COO)_6(TPEB)_6]_n$ (described as **TUS 7**), TPEB = 1,3,5-tris(pyridine-4-ylethynyl)benzene, by reticulating Ag_{12} nodes with a tritopic linker TPEB. Characterized by microscopic and diffraction analyses, the SCAMs revealed distinct morphologies, structural robustness, and phase purity. This paper elucidates how the binding with the organic linkers alters the symmetry of the silver nanoclusters (NCs). Changes in the symmetry of discrete NCs to assembled structures have not been reported yet. This study provides an atomic-level explanation of the transformation of symmetry from NCs to extended structures.

Introduction

Since the pioneering revelation of atom-precise metal nanoclusters (NCs), there has been renewed interest in the domain of nanomaterials.[1–10] The cores of NCs generally exhibit diameters within the range of sub-nanometre to 3 nm and are composed of *ca.* ten to a few hundred metal atoms, which are protected by ligands to stabilize the metal core.[11,12] Worthy of note, NCs display exclusive properties when compared to metal atoms, nanoparticles and the bulk, which can be attributed to the quantum confinement of electrons.[13] Given that metal NCs possess functional diversities in their architecture and their properties are intricately associated with their structure, these unique properties can be correlated to a wide cauldron of applications such as catalysis, sensing, electrochemistry, and biomedicine, among others.[14–17] The core of metal NCs acts as a repository of electrons; some of the coordinating ligands (*e.g.* chloride) withdraw electrons from the core, whereas some other ligands (*e.g.* pyridine and phosphine) simply form coordinated bonds with the metal atoms in the core. Silver (Ag) NCs showcase specific attractive features such as prominent luminescence, catalytic activity, and photon-energy conversion.[15,18,19] However, the lower standard electrode potential of silver ($E°(Ag^+/Ag)$ = 0.79 V) compared to that of gold ($E°(Au^+/Au)$ = 1.83 V) confers Ag NCs with higher propensity to oxidation, which engenders significant obstacles to its practical implementation.[20,21] The major stability concern of Ag NCs has narrowed down the scope of research and applications of these materials in certain domains. Unwavering efforts in the exploration of assembly methods remedied this problem and finally paved the way to the current materials of interest, that is, cluster-assembled materials.[22,23] The functionality of ligands, counter ions or macrocycles was leveraged to self-assemble Ag NCs in order to enhance the stability.[24–26] However, this approach lacks precise control over framework assembly. In the materials arena, the incorporation of organic linkers to bridge metal nodes enabled the construction and functionality of metal–organic frameworks (MOFs), which not only contributed to their enhanced durability but also facilitated charge transfer between metal nodes.[27,28] Driven by the need for long-range extended structures, the concept of organic linkers was imbibed in the assembly of Ag NC

[a]*Department of Applied Chemistry, Faculty of Science, Tokyo University of Science, Kagurazaka, Shinjuku-ku, Tokyo 162-8601, Japan. E-mail: saikatdas@rs.tus.ac.jp*
[b]*Department of Metallurgical Engineering and Materials Science, Indian Institute of Technology Bombay, Mumbai 400 076, India*
[c]*Institute of Multidisciplinary Research for Advanced Materials, Tohoku University, 2-1-1 Katahira, Aoba-ku, Sendai 980-8577, Japan.*
E-mail: yuichi.negishi.a8@tohoku.ac.jp

†Electronic supplementary information (ESI) available. CCDC 2373129 and 2373236. For ESI and crystallographic data in CIF or other electronic format see DOI: https://doi.org/10.1039/d4nr03992k

nodes.[29,30] The cooperative behaviour of Ag NC nodes and organic linkers, along with their interplay, is crucial to the augmented stability, reactivity and functionality of the materials as well as instrumental to their unprecedented properties and functions.

In 2017, Zang *et al.* reported a silver cluster-assembled material (SCAM) that was constructed by coordinating Ag_{12} nodes with bidentate pyridyl linkers.[31] This SCAM, $[Ag_{12}(S^tBu)_8(CF_3COO)_4(bpy)_4]_n$, bpy = 4,4-bipyridine, demonstrated brilliant stability after prolonged exposure to air and visible light irradiation. The following year, Wang and co-workers employed four different linkers (pyrazine, dipyridine-4-yl-diazene, 4,4′-bipyridine, and 1,4-bis(4-pyridyl)benzene) to connect Ag_{14} cores, resulting in four SCAMs (SCAM-1,2,3,4).[32] Notably, SCAM-4 demonstrated commendable thermal stability and also illustrated a broad range (green to red) of thermochromism. Following these pivotal studies, a significant number of SCAMs constituting Ag NC nodes of variable sizes and diverse organic functionalities have been reported.[33–37] SCAMs, composed of different numbers of Ag atoms, *viz*. Ag_{10}, Ag_{12}, Ag_{14}, Ag_{20}, and Ag_{27}, flaunted distinctive structures, which translated to unique properties and performances.[32,37–40] The geometry and connectivity of nodes and linkers dictate the architecture and structural intricacy of SCAMs. Prior reports indicate that SCAMs prepared with pyridine linkers predominantly utilize bidentate and tetradentate linkers, whereas tridentate linkers for SCAM formation have been relatively unexplored.[41] The use of a wide pool of linkers, for instance, 3-amino-4,4′-bipyridine,[42,43] 4,4-azopyridine,[35,44,45] tris(4-pyridylphenyl)amine,[46] 1,4-bis(pyridin-4-ylethynyl)benzene,[47] and 9,10-bis(2-(pyridin-4-yl)vinyl)anthracene[38] to stitch Ag(I) cluster nodes laid the foundation for orchestrating the properties of SCAMs constructed by means of diverse synthesis strategies such as one-pot synthesis, liquid–liquid interfacial crystallization and ligand-exchange.[31,39] Despite significant strides in the designed synthesis of SCAMs, the assembly mechanism from the perspective of the symmetry of the linkers transforming the original symmetry of the nanocluster's core–shell architecture into a new anisotropic symmetry of the extended networks has not been unravelled yet.

In this work, we accomplished the precise coordination of Ag_{12} nodes and organic linkers into well-ordered, crystalline 3D and 2D SCAM structures. This is the first report of a

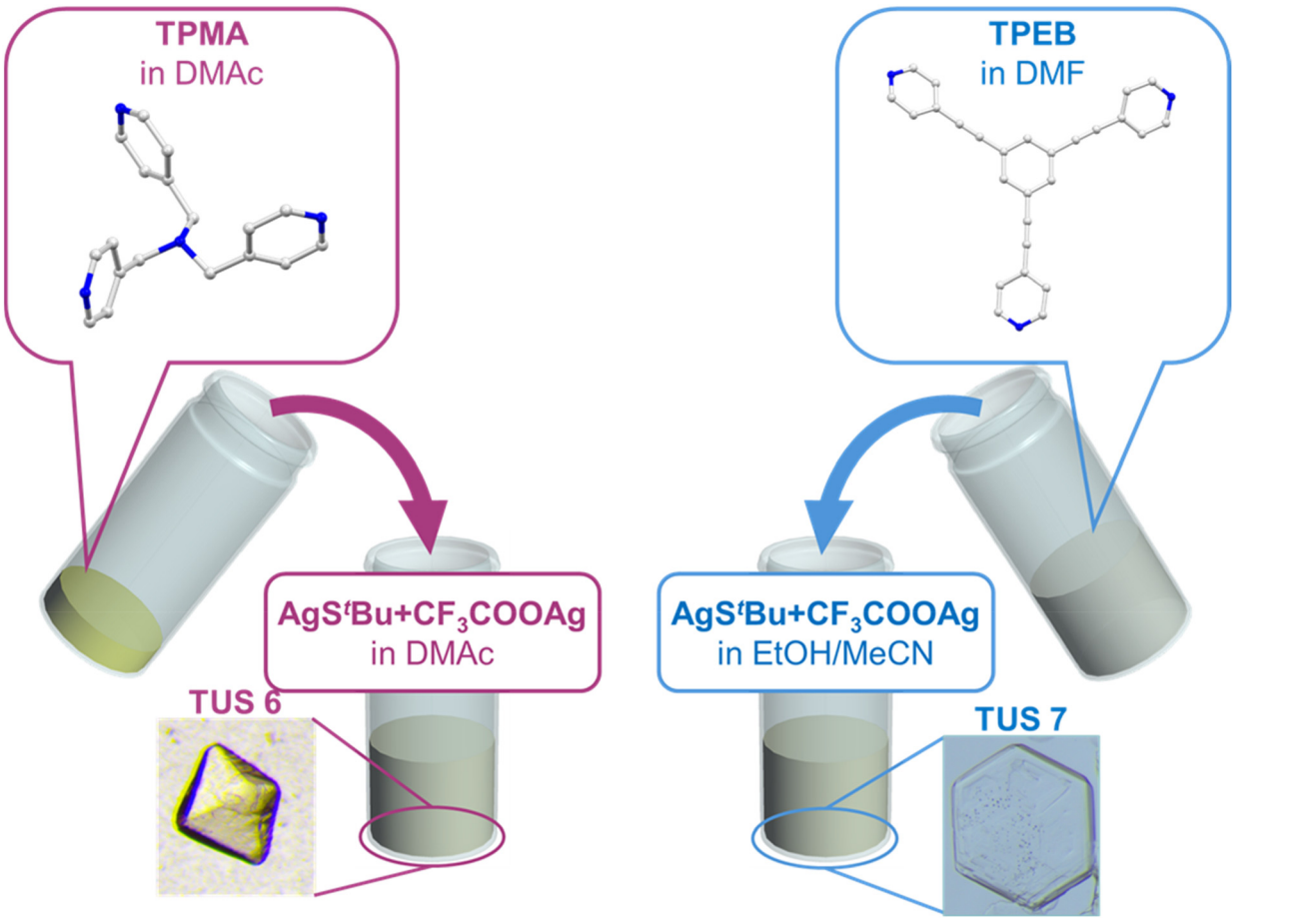

Fig. 1 Schematic depicting the preparation of **TUS 6** and **TUS 7** single crystals. The optical microscopy images of the single crystals are shown as enlarged views of the encircled portions at the product vial bottoms. Color code: N, blue; C, grey. H atoms are removed for clarity.

(3,6)-connected 3D SCAM, $[Ag_{12}(S^tBu)_6(CF_3COO)_6(TPMA)_6]_n$ (**TUS 6**), TPMA = tris(pyridine-4-ylmethyl)amine, utilizing a tridentate linker TPMA. In addition to **TUS 6**, another 2D SCAM, $[Ag_{12}(S^tBu)_6(CF_3COO)_6(TPEB)_6]_n$ (**TUS 7**), TPEB = 1,3,5-tris(pyridine-4-ylethynyl)benzene, was developed by bridging Ag_{12} nodes with a different tridentate linker TPEB. By optimizing the crystallization conditions, we achieved controllable dimensionality of SCAMs endowed with high-quality, well-defined crystalline structures. This study imparts with comprehensive insights into the transformation of the isotropic two-fold symmetry of the NC's core–shell structure to an anisotropic six-fold symmetry of assembled structures.

Results and discussion

Single crystals of **TUS 6** were prepared utilizing a facile optimized reaction at ambient temperature. The reaction was initiated by sequentially adding $[AgS^tBu]_n$ and CF_3COOAg to an *N*,*N*′-dimethylacetamide (DMAc) solution and stirring the reaction mixture. Meanwhile, the tris(pyridine-4-ylmethyl)amine (TPMA) linker was also dissolved in DMAc. After this, the linker solution was added dropwise into the vessel containing the solution of metal precursors and then allowed to stand for crystallization. After 1 day, colorless octahedral-shaped crystals as observed from the optical microscopy images were obtained from the bottom of the solution in 40.6% yield based on Ag (Fig. 1 and S1a†). In order to characterize the crystals, single-crystal X-ray diffraction (SCXRD) measurement and analysis were conducted to scrutinize the crystallographic structure of the SCAM in vivid detail. As can be seen from the results of SCXRD analysis, **TUS 6** is crystallized in an orthorhombic crystal system and the space group is *Pbca* (no. 61) (Table S1†). From the viewpoint of cluster nodes in detail, each node consists of a Ag_{12} core that can be illustrated as a hollow cuboctahedron (Fig. 2a). The core can be segregated into three layers; the middle hexagonal layer consisting of six Ag atoms is present between two triangular layers. Regarding the upper and lower triangular layers, the Ag–Ag bond lengths range from 2.936 Å to 2.961 Å. Considering that the Ag–Ag bonding between the middle hexagonal layer and the upper and lower triangular layers assist in maintaining the skeleton, these Ag–Ag distances lie between 3.001 Å and 3.044 Å (Fig. S2 and Table S3†). These lengths are shorter than twice the van der Waals radius of silver (3.44 Å), which is indicative of argentophilic interactions between silver atoms.[48] Focusing on stabilizing ligands, there are six *tert*-butyl thiolate (–S^tBu) ligands. Six S atoms belonging to S^tBu molecules construct the cluster nodes and each of them connects four different Ag atoms (located at the vertices of the trapezoidal faces building the cuboctahedron) in μ_4-η^1, η^1, η^1, η^1 ligation (Fig. 2b and S4†). The distances between Ag and S atoms fall within the range of 2.476 Å to 2.538 Å (Fig. S3 and Table S5†). Going into further detail, six trifluoroacetate (–CF_3COO^-) ligands protect the cluster nodes *via* O atoms (Fig. 2c). Four of the six CF_3COO^- ligands connect two different Ag atoms by utilizing two O atoms (μ_2-η^1, η^1) (Fig. S6(a)†) and the other two CF_3COO^- ligands connect to only one Ag atom by harnessing one oxygen atom (μ_1-η^1) (Fig. S6(b)†). The Ag–O distances fall between 2.384 Å and 2.710 Å (Fig. S5 and Table S7†). Furthermore, we draw attention to the coordination between the cluster nodes and TPMA linker molecules. Each Ag NC node connects six different linker molecules through six Ag atoms, which exist in the middle hexagonal layer (Fig. 2d). The distances between Ag and N atoms (pertaining to the pyridine linker) fall in the range of 2.268 Å to 2.298 Å (Fig. S7 and Table S9†). To comprehend the Ag–linker connectivities more minutely, we illustrated the coordination pattern where each coordinating linker alternately orients upward or downward, thereby resulting in three connectivities pointing upwards and three downwards (Fig. 2e and S8†). Overall, the assembled structure can be denoted as $[Ag_{12}(S^tBu)_6(CF_3COO)_6(TPMA)_6]$, where the tritopic feature of the flexible TPMA linker allows it to reticulate with

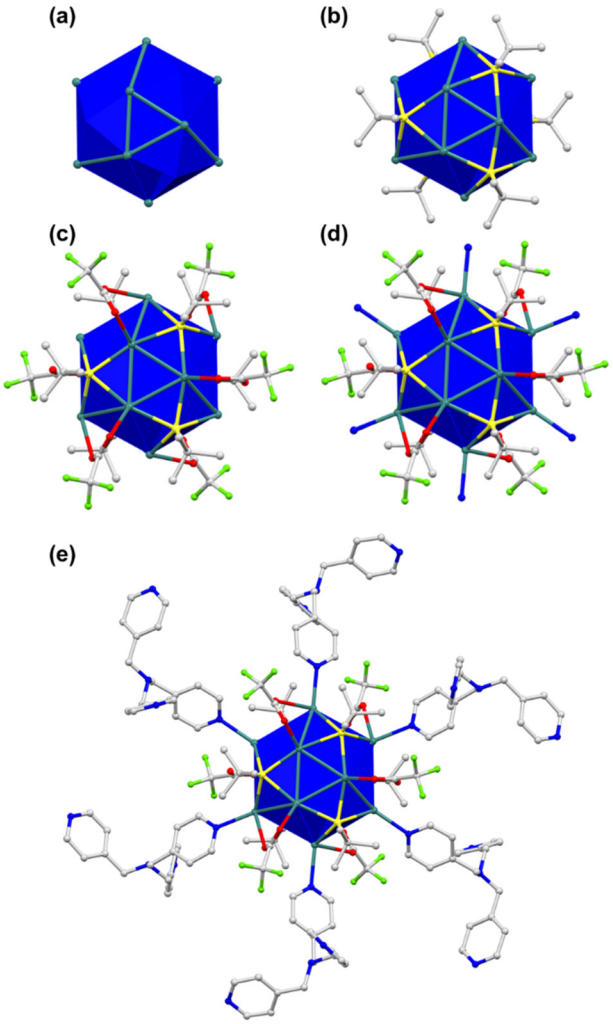

Fig. 2 Simplified sequential development of Ag_{12} cluster nodes and their connectivities in **TUS 6**: (a) cluster core comprising 12 Ag atoms and protected by (b) six –S^tBu ligands and (c) six –CF_3COO ligands. (d) N sites and (e) the corresponding organic linkers coordinated to the Ag_{12} nodes. H atoms are removed for clarity.

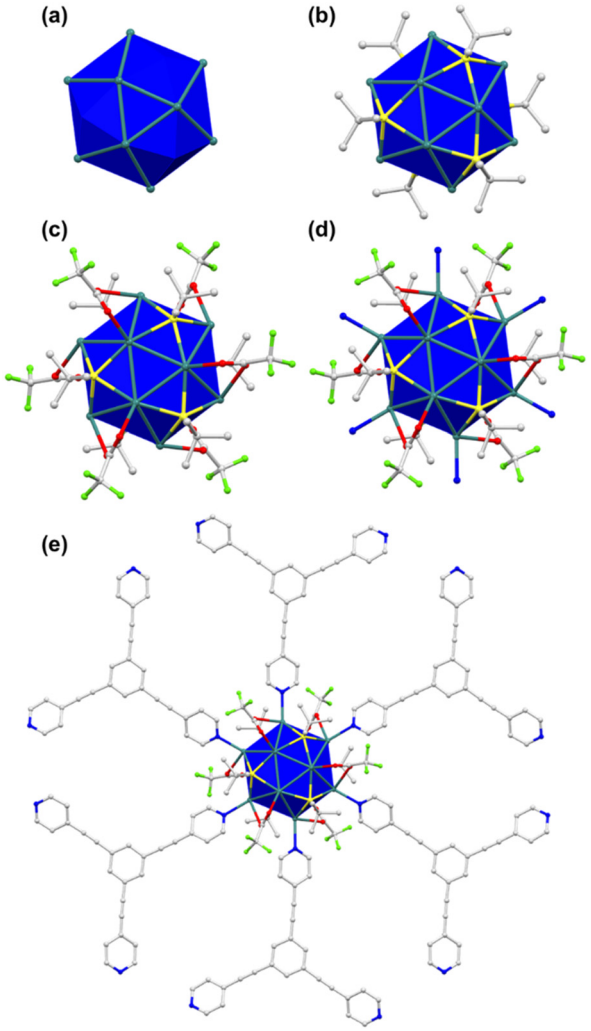

Fig. 3 Sequence of designing Ag_{12} cluster nodes and their connectivities in **TUS 7**: (a) Ag_{12} cluster core stabilized by (b) six $-S^tBu$ ligands and (c) six $-CF_3COO$ ligands. (d) N sites and (e) the corresponding organic linkers coordinated to the Ag_{12} nodes. H atoms are removed for clarity.

three adjacent Ag NC nodes and each node is connected to six different TPMA linkers, yielding a 3D architectural network represented as **TUS 6** (Fig. 4).

In order to investigate whether the flexibility of the linkers contributes to the SCAM structure, we reticulated a rigid linker, 1,3,5-tris(pyridine-4-ylethynyl)benzene (TPEB), with Ag NC vertices to afford single crystals of **TUS 7**. Regarding the preparation of **TUS 7**, $[AgS^tBu]_n$ and CF_3COOAg were also utilized as metal precursors and dissolved in acetonitrile/ethanol (MeCN/EtOH) (v/v = 1 : 1). Meanwhile, the TPEB linker was dissolved in dimethylformamide (DMF). Following this, the linker solution was added to the metal precursor solution. After leaving undisturbed for 1 day, colorless hexagonal-shaped crystals were collected from the bottom of the solution mixture in 69.6% yield based on TPEB (Fig. 1 and S1b†).

Close examination of the crystallographic structure of **TUS 7** revealed that it crystallized in a trigonal system with a space

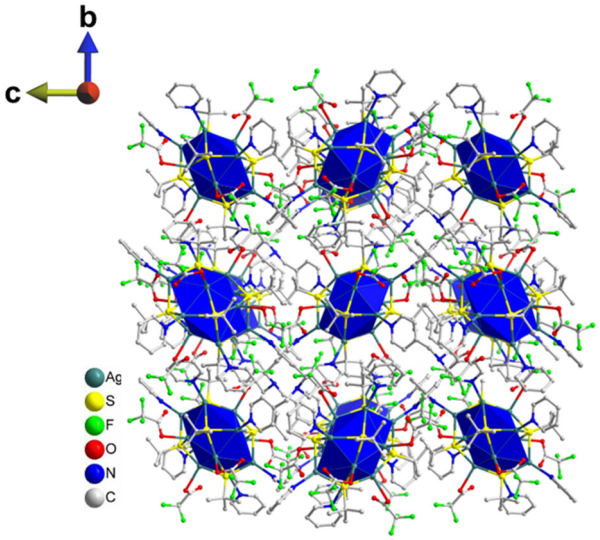

Fig. 4 Extended framework of **TUS 6**. H atoms are removed for clarity.

group of $R\bar{3}$ (no. 148) (Table S2†). Although the Ag_{12} cluster core of **TUS 7** resembles that of **TUS 6** in shape, the Ag–Ag, Ag–CF_3COO^- and Ag–N connectivity patterns differ between the two. The two triangular planes above and beneath the intermediate hexagonal layer are equilateral in nature, with the Ag–Ag bond distance measuring 3.020 Å. The connection between the Ag atom(s) present in the triangular plane(s) and the Ag atom(s) present in the middle hexagonal plane alternately display bond lengths of 3.104 Å and 3.228 Å (Fig. 3a, S9 and Table S11†). Since all of the Ag–Ag bond lengths are less than twice the van der Waals radius of Ag, we can categorize the Ag–Ag interactions as argentophilic. The four Ag atoms located on the vertices of the trapezoidal plane formed by two Ag atoms

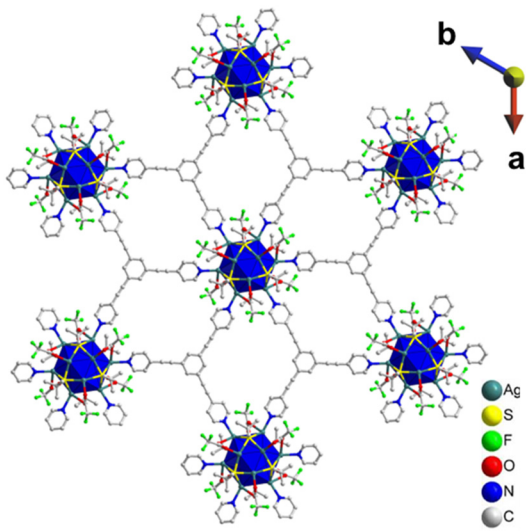

Fig. 5 2D layered structure of **TUS 7** where each layer is formed through the coordinate bonding between Ag_{12} NC vertices and TPEB linkers. H atoms are removed for clarity.

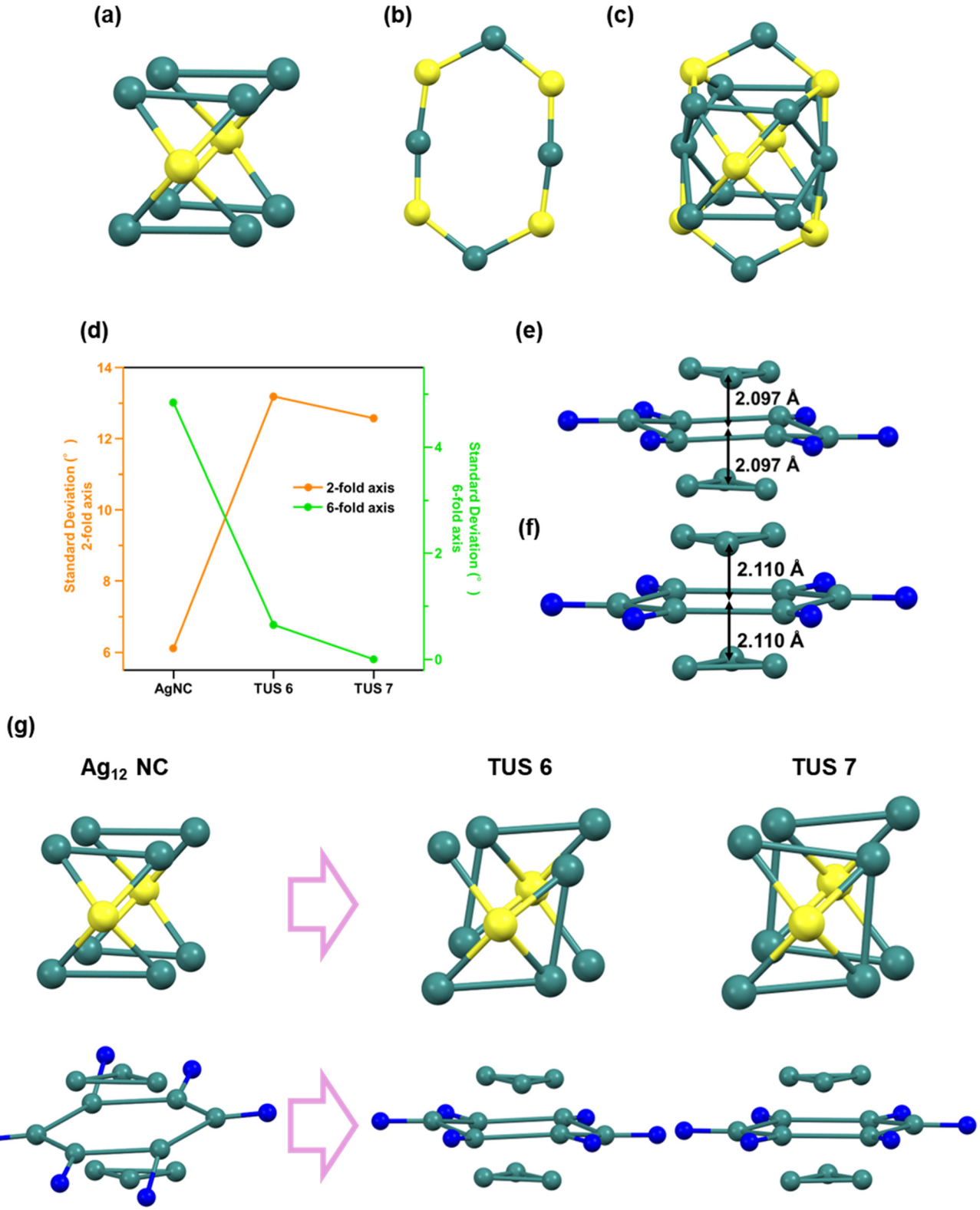

Fig. 6 (a) Ag_8 cuboid core and (b) Ad_4S_4 hexagonal shell forming the (c) Ag_{12} NC. (d) Standard deviation in the corner angles of the Ag_8 cuboid core structure and Ag_6 middle layer. Ag_3–Ag_6–Ag_3 trilayered structures of (e) **TUS 6** and (f) **TUS 7**. (g) Transformation from the isotropic two-fold symmetry of the NC's core–shell architecture and core to an anisotropic six-fold symmetry originating from the linker-induced stress.

from the top/bottom plane and two atoms from the middle plane are connected to each S atom of the six –S^{t}Bu stabilizing ligands by μ_4-η^1, η^1, η^1, η^1 ligation (Fig. S11†), featuring Ag–S bond lengths that span from 2.471 Å to 2.544 Å (Fig. 3b, S10 and Table S13†). Six CF_3COO^- ligands protect the cluster core, and all of these ligands connect to two Ag atoms, one from the triangular layers and another from the hexagonal layer, by utilizing two O atoms (μ_2-η^1, η^1) (Fig. S13†). The Ag–O bond distance for Ag atoms in the upper or lower layers is 2.401 Å, whereas the corresponding distance for Ag atoms in the intermediate layer is 2.684 Å (Fig. 3c, S12 and Table S15†). Furthermore, the cluster–linker reticulation led to an equal Ag–N bond distance of 2.275 Å (Fig. 3d, S14 and Table S17†). The relatively rigid TPEB linkers reticulate with Ag_{12} NC nodes (Fig. 3e), generating a 2D 3,6-connected layered structure of **TUS 7** (Fig. 5). **TUS 7** exhibits an *ABC* stacking arrangement where the interlayer distance measures 7.063 Å (Fig. S15†).

The structure of many metal NCs generally consists of a highly isotropic core and a shell (or staple) that stabilizes it, forming a stable core–shell structure. As can be seen from Fig. 6c, the structure of Ag_{12} NCs[31] comprises an Ag_8 cuboid core (Fig. 6a) and an Ag_4S_4 hexagonal shell (Fig. 6b). The small variation in the corner angles of the cuboid core structure indicates that the Ag_8 cuboid core closely resembles a cuboid and exhibits a highly isotropic structure (Fig. 6d). This core structure possesses a two-fold symmetry axis. However, as the assembly method progresses, this isotropy and two-fold symmetry decrease, while anisotropy increases, originating from

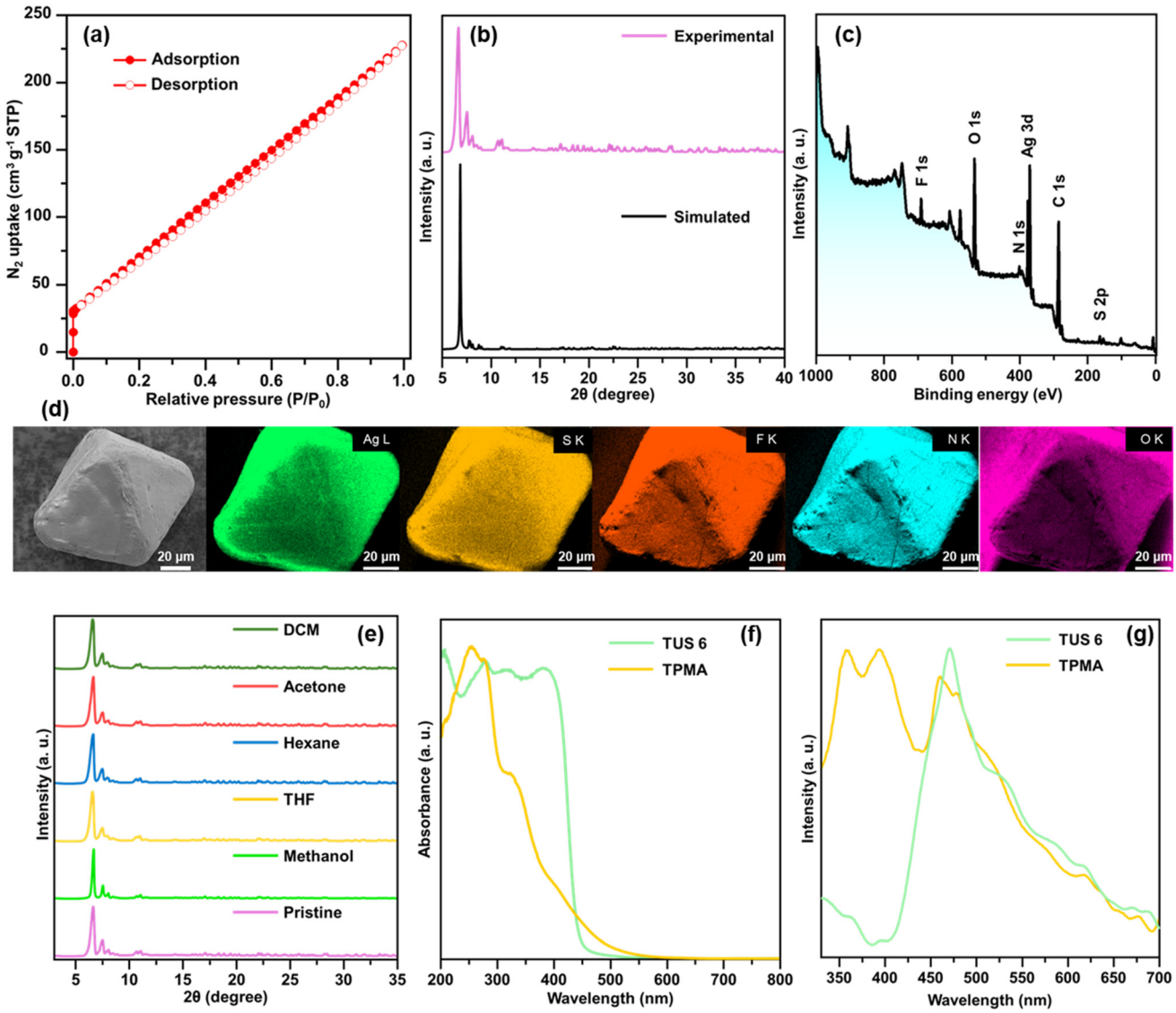

Fig. 7 (a) N_2 physisorption isotherms, (b) experimentally obtained and simulated PXRD profiles, (c) XPS survey spectra, (d) SEM micrograph and the corresponding EDX elemental mapping analyses, (e) PXRD profiles after treating in various solvents, (f) DRS spectra, and (g) photoluminescence (PL) spectrum of **TUS 6**.

the stress induced by the linker on the nanocluster site and the symmetry (hexagonal symmetry) and distortion-derived anisotropy.

The structure of the SCAM nanocluster discards the Ag_8 cuboid core and transforms to a highly anisotropic Ag_3–Ag_6–Ag_3 trilayered structure (Fig. 6e and f). Accompanying this collapse of isotropy, the stress from the linker's symmetry affects the NC site in the SCAM, altering the original NC symmetry. In **TUS 7**, since the linker is of D_{3h} symmetry, the symmetric stress from it acts on the NC site, causing the loss of the two-fold symmetry axis and the emergence of a six-fold symmetry axis in the Ag_6 middle layer (indicated by the blue trace in Fig. S16†). In **TUS 6**, as the linker is of C_{3v} symmetry and lacks a symmetry plane perpendicular to the three-fold rotational axis, it retains slight two-fold symmetry but adopts a structure close to six-fold symmetry (red trace in Fig. S16†). This is evident from the variation in the corner angles of the Ag_6 middle layer, where the hexagonal angles are extremely small in both **TUS 6** and **TUS 7**, but very large in the NC (green trace in Fig. 6d). Additionally, the variation in the corner angles of the Ag_8 cuboid core mentioned earlier is very small in the NC but large in the SCAMs (orange trace in Fig. 6d). Therefore, it can be concluded that the assembly process entails the collapse of the isotropic two-fold symmetry of the nanocluster's core–shell structure and core, and the formation of new anisotropic six-fold symmetry derived from the linker-induced stress (Fig. 6g).

Structural characterization of the SCAMs was conducted using different analytical techniques. The specific surface areas of the SCAMs were assessed by degassing the adsorbents at a temperature of 50 °C for 8 hours, followed by recording the N_2 adsorption/desorption isotherms under 77 K over the relative pressure (P/P_0) range of 0–1. Type-I isotherms were observed, characterized by their concavities to the P/P_0 axis and a steep rise in N_2 uptake at very low relative pressures (Fig. 7(a) and 8(a)). Application of the Brunauer–Emmett–

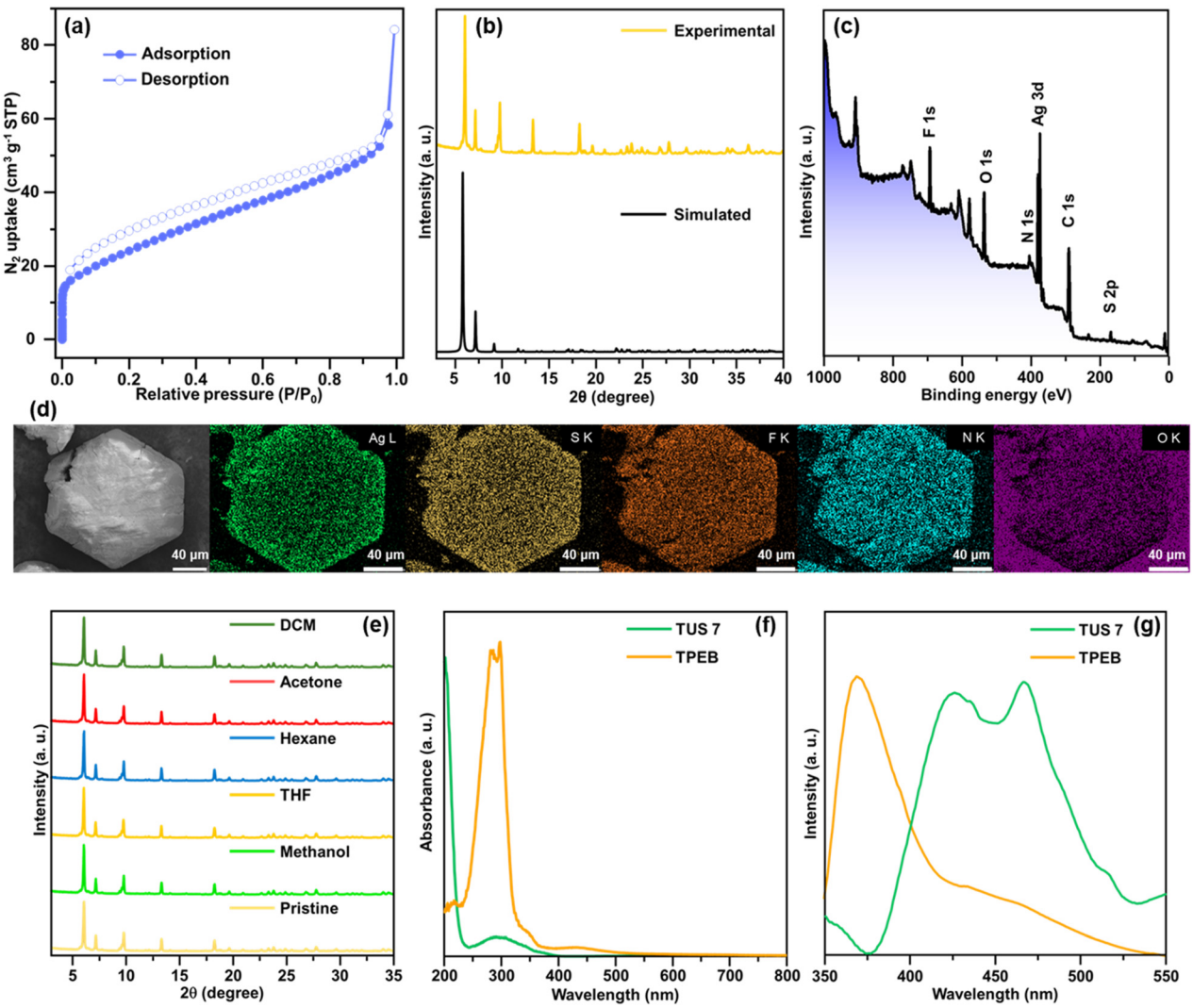

Fig. 8 (a) N_2 physisorption isotherms, (b) experimentally obtained and simulated PXRD profiles, (c) XPS survey spectra, (d) SEM micrograph and the corresponding EDX elemental mapping analyses, (e) PXRD profiles after treating in various solvents, (f) DRS spectra, and (g) PL spectrum of **TUS 7**.

Teller (BET) equation furnished specific surface areas of 330.2 and 88.4 $m^2\ g^{-1}$ for **TUS 6** and **TUS 7**, respectively (Fig. S17 and S18†). To evaluate the phase purity of **TUS 6** and **TUS 7** crystals, we performed PXRD and compared with simulation results generated from SCXRD analyses. Reasonable matching was observed that implied the preservation of structural crystallinity even after the removal of the mother solvents (Fig. 7b and 8b). Optical microscopy and scanning electron microscopy (SEM) inspection divulged distinct morphologies for the SCAMs. Octahedral and hexagonal-shaped crystals were observed for **TUS 6** and **TUS 7**, respectively (Fig. 7d and 8d). After this, we explored the elemental composition and electronic structures of the SCAMs *via* X-ray photoelectron spectroscopy (XPS). As evident from the survey spectra (Fig. 7c and 8c), the presence of Ag, S, N, F, and O could be traced, which was found to be in agreement with the energy dispersive X-ray (EDX) findings (Fig. 7d and 8d). To scrutinise in more detail, high-resolution XPS measurements were undertaken for each element to observe their respective electronic states (Fig. S19 and S20†). The Ag peaks detected at 373.7 and 374.4 eV for **TUS 6** and **TUS 7**, respectively, can be attributed to Ag $3d_{3/2}$. On the other hand, the peaks at 367.6 and 368.4 eV for **TUS 6** and **TUS 7**, respectively, correspond to Ag $3d_{5/2}$. The splitting of 6.0 eV between the Ag $3d_{3/2}$ and Ag $3d_{5/2}$ peaks validated that the oxidation state of Ag is +1 for both the SCAMs. The S binding energy spectra showcased two peaks: 162.5 and 161.3 eV for **TUS 6** and 163.6 and 162.3 eV for **TUS 7**, which can be traced to S $2p_{1/2}$ and S $2p_{3/2}$, respectively. These binding energies corroborate the existence of Ag–S–C bonds. Additionally, the collected O 1s binding energy spectra revealed peaks at 530.8 eV for **TUS 6** and 531.4 eV for **TUS 7**, which substantiate the formation of Ag–O bonds. Regarding the N 1s spectra, the peaks were located at 398.8 eV (**TUS 6**) and 399.4 eV (**TUS 7**), reinforcing the presence of coordination bonds between silver clusters and linkers. Next, we screened the stability of the SCAMs against different solvents, which attested to their high chemical stabilities (Fig. 7e and 8e). To assess the thermal stabilities at elevated temperatures, the SCAMs were subjected to thermogravimetric analysis (TGA). No appreciable thermal decomposition of the SCAMs could be detected before 120 °C, reflective of substantial improvements in structural robustness against temperature relative to discrete Ag NCs[38] (Fig. S21 and S22†). PXRD analyses of the SCAMs after heating at different temperatures also corroborated the maintenance of the crystalline structures up to 120 °C (Fig. S23 and S24†).

Diffuse reflectance spectroscopy (DRS) measurements revealed that TPMA exhibited a pronounced absorption peak at around 255 nm and a small peak at 325 nm. In contrast, **TUS 6** displayed peaks at approximately 200, 280, 325, and 385 nm (Fig. 7f). The shift in the absorbance of **TUS 6** from that of the TPMA linker suggests that the observed peak arises exclusively from the SCAM structure and not only from the linker. Upon excitation at 255 nm, a pronounced PL emission peak was detected at 471 nm, which could be assigned to the TPMA linker (Fig. 7g). Comparative analysis of the DRS spectra for TPEB and **TUS 7** demonstrated that TPEB features absorption maxima around 285 nm and 300 nm. On the other hand, **TUS 7** exhibited a strong peak around 200 nm and a weaker peak around 300 nm (Fig. 8f). In the case of the TPEB solid, the PL peak at 370 nm originates from the linker, and the shoulder peak around 450 nm may correspond to the excimer emission of TPEB (Fig. 8g). When excited at 298 nm, **TUS 7** exhibited emission maxima at 426 and 466 nm. In **TUS 7**, the PL peaks around 400–500 nm can be assigned to enhanced excimer emission from the stacked linker. As a result, the PL in **TUS 6** and **TUS 7** arises from their linkers. Based on these observations, it can be inferred that the generation of the SCAM leads to significant changes in the peak shapes, indicative of alterations in electronic states brought about by the formation of the extended structures.

Conclusions

In summary, this study demonstrates the assembly of dodecanuclear Ag(I) cluster nodes with tritopic pyridine linkers TPEB and TPMA to furnish two intricate and extended SCAM networks **TUS 6** and **TUS 7**. Remarkably, **TUS 6** exemplifies the first three-periodic SCAM net built with a tritopic linker. Characterization techniques successfully revealed the unique crystalline structure of these SCAMs, exhibiting high phase purity and pronounced stability, which was accomplished by optimizing the synthesis route of the SCAMs. This contribution sheds light on the precise architecture of SCAMs at the atomic scale, discussing how the assembly mechanism results in the collapse of the isotropic two-fold symmetry of the core–shell structure and core of the nanoclusters and the generation of a new anisotropic six-fold symmetry arising from the stress induced by the linker on the nanocluster site. These insights offer a guideline for designing novel reticular architectures by regulating the coordination geometry of the metal clusters and the symmetry of the organic linkers.

Author contributions

R. N.: synthesis, characterization, and manuscript writing. J. S.: synthesis and characterization. A. S.: characterization and manuscript writing. A. K.: characterization. R. T.: characterization. T. K.: characterization. S. D.: conceptualization, project supervision, and manuscript writing. Y. N.: project supervision and funding acquisition.

Data availability

The data supporting this article have been included as part of the ESI.† Crystallographic data for $[Ag_{12}(S^tBu)_6(CF_3COO)_6(TPMA)_6]_n$ and $[Ag_{12}(S^tBu)_6(CF_3COO)_6(TPEB)_6]_n$ have been deposited at the CCDC under CCDC numbers 2373129 and 2373236, respectively.†

Conflicts of interest

There are no conflicts to declare.

Acknowledgements

This study was supported by the JSPS KAKENHI (grant no. 20H02698, 20H02552), the Ogasawara Foundation for the Promotion of Science and Engineering, the Yazaki Memorial Foundation for Science and Technology, and "Aquatic Functional Materials" (grant no. 22H04562).

References

1 I. Chakraborty and T. Pradeep, *Chem. Rev.*, 2017, **117**, 8208–8271.
2 C. M. Aikens, *Acc. Chem. Res.*, 2018, **51**, 3065–3073.
3 Z. Wang, R. K. Gupta, G.-G. Luo and D. Sun, *Chem. Rec.*, 2020, **20**, 389–402.
4 R. Jin, C. Zeng, M. Zhou and Y. Chen, *Chem. Rev.*, 2016, **116**, 10346–10413.
5 Y. Du, H. Sheng, D. Astruc and M. Zhu, *Chem. Rev.*, 2020, **120**, 526–622.
6 P. Maity, S. Xie, M. Yamauchi and T. Tsukuda, *Nanoscale*, 2012, **4**, 4027–4037.
7 Q. Yao, Z. Wu, Z. Liu, Y. Lin, X. Yuan and J. Xie, *Chem. Sci.*, 2021, **12**, 99–127.
8 H. Qian, M. Zhu, Z. Wu and R. Jin, *Acc. Chem. Res.*, 2012, **45**, 1470–1479.
9 S. Biswas, S. Das and Y. Negishi, *Nanoscale Horiz.*, 2023, **8**, 1509–1522.
10 A. Ghosh, O. F. Mohammed and O. M. Bakr, *Acc. Chem. Res.*, 2018, **51**, 3094–3103.
11 R. Jin, *Nanoscale*, 2015, **7**, 1549–1565.
12 Y. Lu and W. Chen, *Chem. Soc. Rev.*, 2012, **41**, 3594–3623.
13 X. Du and R. Jin, *Dalton Trans.*, 2020, **49**, 10701–10707.
14 M. G. Méndez-Medrano, E. Kowalska, A. Lehoux, A. Herissan, B. Ohtani, D. Bahena, V. Briois, C. Colbeau-Justin, J. L. Rodríguez-López and H. Remita, *J. Phys. Chem. C*, 2016, **120**, 5143–5154.
15 T. Udaya Bhaskara Rao and T. Pradeep, *Angew. Chem., Int. Ed.*, 2010, **49**, 3925–3929.
16 K. Sun, Y. Fu, T. Sekine, H. Mabuchi, S. Hossain, Q. Zhang, D. Liu, S. Das, D. He and Y. Negishi, *Small*, 2024, **20**, 2304210.
17 L. Shang, S. Dong and G. U. Nienhaus, *Nano Today*, 2011, **6**, 401–418.
18 M. Urushizaki, H. Kitazawa, S. Takano, R. Takahata, S. Yamazoe and T. Tsukuda, *J. Phys. Chem. C*, 2015, **119**, 27483–27488.
19 Y. Niihori, Y. Wada and M. Mitsui, *Angew. Chem., Int. Ed.*, 2021, **60**, 2822–2827.
20 W. M. Haynes, *Handbook of Chemistry and Physics*, CRC Press, 93rd edn, 2012.
21 R. P. A. J. Bard and J. Jordan, *Standard Potentials in Aqueous Solution*, CRC Press, 1985.
22 X. Kang and M. Zhu, *Coord. Chem. Rev.*, 2019, **394**, 1–38.
23 S. Biswas, P. Sun, X. Xin, S. Mandal and D. Sun, in *Atomically Precise Nanochemistry*, 2023, pp. 453–478. DOI: 10.1002/9781119788676.ch15.
24 Z.-Y. Chen, D. Y. S. Tam, L. L.-M. Zhang and T. C. W. Mak, *Chem. – Asian J.*, 2017, **12**, 2763–2769.
25 Z. Wang, X.-Y. Li, L.-W. Liu, S.-Q. Yu, Z.-Y. Feng, C.-H. Tung and D. Sun, *Chem. – Eur. J.*, 2016, **22**, 6830–6836.
26 A. Mathew, G. Natarajan, L. Lehtovaara, H. Häkkinen, R. M. Kumar, V. Subramanian, A. Jaleel and T. Pradeep, *ACS Nano*, 2014, **8**, 139–152.
27 O. M. Yaghi, M. O'Keeffe, N. W. Ockwig, H. K. Chae, M. Eddaoudi and J. Kim, *Nature*, 2003, **423**, 705–714.
28 S. Kitagawa, R. Kitaura and S.-i. Noro, *Angew. Chem., Int. Ed.*, 2004, **43**, 2334–2375.
29 Z.-Y. Wang and S.-Q. Zang, in *Atomically Precise Nanochemistry*, 2023, pp. 479–501. DOI: 10.1002/9781119788676.ch16.
30 S. Biswas and Y. Negishi, *Chem. Rec.*, 2024, **24**, e202400052.
31 R.-W. Huang, Y.-S. Wei, X.-Y. Dong, X.-H. Wu, C.-X. Du, S.-Q. Zang and T. C. W. Mak, *Nat. Chem.*, 2017, **9**, 689–697.
32 Z.-Y. Wang, M.-Q. Wang, Y.-L. Li, P. Luo, T.-T. Jia, R.-W. Huang, S.-Q. Zang and T. C. W. Mak, *J. Am. Chem. Soc.*, 2018, **140**, 1069–1076.
33 M. Cao, R. Pang, Q.-Y. Wang, Z. Han, Z.-Y. Wang, X.-Y. Dong, S.-F. Li, S.-Q. Zang and T. C. W. Mak, *J. Am. Chem. Soc.*, 2019, **141**, 14505–14509.
34 M. J. Alhilaly, R.-W. Huang, R. Naphade, B. Alamer, M. N. Hedhili, A.-H. Emwas, P. Maity, J. Yin, A. Shkurenko, O. F. Mohammed, M. Eddaoudi and O. M. Bakr, *J. Am. Chem. Soc.*, 2019, **141**, 9585–9592.
35 A. K. Das, S. Biswas, S. S. Manna, B. Pathak and S. Mandal, *Inorg. Chem.*, 2021, **60**, 18234–18241.
36 W. A. Dar, A. Jana, K. S. Sugi, G. Paramasivam, M. Bodiuzzaman, E. Khatun, A. Som, A. Mahendranath, A. Chakraborty and T. Pradeep, *Chem. Mater.*, 2022, **34**, 4703–4711.
37 M. Zhao, S. Huang, Q. Fu, W. Li, R. Guo, Q. Yao, F. Wang, P. Cui, C.-H. Tung and D. Sun, *Angew. Chem., Int. Ed.*, 2020, **59**, 20031–20036.
38 T. Sekine, J. Sakai, Y. Horita, H. Mabuchi, T. Irie, S. Hossain, T. Kawawaki, S. Das, S. Takahashi, S. Das and Y. Negishi, *Chem. – Eur. J.*, 2023, **29**, e202300706.
39 R. Nakatani, S. Biswas, T. Irie, J. Sakai, D. Hirayama, T. Kawawaki, Y. Niihori, S. Das and Y. Negishi, *Nanoscale*, 2023, **15**, 16299–16306.
40 J.-Y. Wang, J.-W. Yuan, X.-M. Liu, Y.-J. Liu, F. Bai, X.-Y. Dong and S.-Q. Zang, *Aggregate*, 2024, **5**, e508.
41 R. Nakatani, S. Das and Y. Negishi, *Nanoscale*, 2024, **16**, 9642–9658.
42 X.-H. Ma, J.-Y. Wang, J.-J. Guo, Z.-Y. Wang and S.-Q. Zang, *Chin. J. Chem.*, 2019, **37**, 1120–1124.

43 X.-Y. Dong, Y. Si, J.-S. Yang, C. Zhang, Z. Han, P. Luo, Z.-Y. Wang, S.-Q. Zang and T. C. W. Mak, *Nat. Commun.*, 2020, **11**, 3678.
44 S. Biswas, A. K. Das, A. Nath, S. Paul, M. Suheshkumar Singh and S. Mandal, *Nanoscale*, 2021, **13**, 17325–17330.
45 A. K. Das, S. Biswas, A. Thomas, S. Paul, A. S. Nair, B. Pathak, M. S. Singh and S. Mandal, *Mater. Chem. Front.*, 2021, **5**, 8380–8386.
46 X.-S. Du, B.-J. Yan, J.-Y. Wang, X.-J. Xi, Z.-Y. Wang and S.-Q. Zang, *Chem. Commun.*, 2018, **54**, 5361–5364.
47 S. Das, T. Sekine, H. Mabuchi, S. Hossain, S. Das, S. Aoki, S. Takahashi and Y. Negishi, *Chem. Commun.*, 2023, **59**, 4000–4003.
48 H. Schmidbaur and A. Schier, *Angew. Chem., Int. Ed.*, 2015, **54**, 746–784.